npj | clean water

www.nature.com/npjcleanwater

ARTICLE OPEN

Check for updates

A resonant electro-physical transmutation method for water purification

McKane B. Lee[1]✉, Nicholas D. Ward[2], Michael Leach[3] and Randy Kent[3]

We present an electro-transmutation (ET) method of water purification using the Quantum Kinetic Fusor™. Electrolysis experiments were performed with residential well water and seawater coupled with two different electrode materials—stainless steel and aluminum—to test the effectiveness of ET in removing contaminants and altering the physiochemistry (e.g., pH, alkalinity) and isotopic composition of water. ET effectively removed contaminants at power inputs as low 0.142 mA cm^{-2}, i.e., 1.9–4.2 watts, which is substantially lower than other electrochemical techniques. The ET process also reduces, and in some cases eliminates, electrode surface area degradation. This outcome is outside the field of traditional Faraday electrolysis, further distinguishing the ET process as potentially more cost-effective than other water purification methods. Importantly, the experiments reveal ET is an exceptionally low input energy generator. This finding is based on the presence of exotic x-rays (Bremsstrahlung) emissions during operation (1–20 KeV).

npj Clean Water (2022)5:35 ; https://doi.org/10.1038/s41545-022-00179-w

INTRODUCTION

Water purification is a technique broadly used for wastewater treatment, industrial processing, residential applications, medical treatment, and radioactive wastewater treatment[1]. There are many types of water purification methods including simple submerged electrolysis to complex direct current regulated power supplies to electrode potential passivation, degasification, chemical filtration, active carbon, anode consumption, cell REDOX potentials, active chlorine, ultrasonic sound devices, ultraviolet light stimulation, peroxi-coagulation, adsorption methods[2], filtration, reverse osmosis, advanced membrane systems, sedimentation and a wide range of gaseous matter vessel reactions. These different methods are used to target specific types of contaminants for varying applications and have inherently different energy and resource costs.

As global temperatures continue to rise due to increasing atmospheric CO_2 levels and the world's natural resources dwindle, it is becoming increasingly important to develop water purification technologies that require minimal energy and natural resource costs. As recently as 2020, scientists studying electron bifurcation in nature made a clarion call for the building of synthetic electron manipulating machines to answer the need for clean, sustainable energy technologies[3].

This study aims to explore the utility of one such device—the Quantum Kinetic Fusor™ (QKF). The system uses voltage in a purely physical process, without re-sorting to passing current through an electrolyte in a chemical interaction. The tri-coil design resonant cavity transformer uses the dielectric properties of a material acting as part of a resonant closed-loop electrical (Resistor, Inductor, Capacitor) RLC tank circuit. The tri-coil transformer (or TCT) is tuned to resonance with the dielectric properties of a suitable material, which can be water, liquid metals, ambient air or even the vacuum of space. The TCT can be a tri-coil resonating cavity transformer employing either a Maxwell or Helmholtz tri-coil design. The physical approach to electrolysis is based on voltage and not amperage to dissociate a selected dielectric medium, an approach that is 180 degrees out of phase from traditional Faraday electrolysis.

As suggested in this research, the QKF™ is an energy-efficient device that removes an array of contaminants from water, including strontium, which has historically proved resistant to traditional purification methods (Fig. 1). The carbon footprint appears to be ~99.7% lower than prior electrolyte devices. Prior art dissociation of water occurs typically between 10 and 350 mA cm^{-2} depending on the methods employed[4]. The disclosed device successfully dissociates water between 0.146 and 0.366 mA cm^{-2} (1.9–4 watts). With such low power consumption, this device can be operated with a 20–50 watt solar panel/charge controller and a 12 V battery. The only substantial carbon footprint is associated with manufacturing the device (machining, lathe, source material, etc.).

During operation of the QKF, the primary challenge is maintaining resonance with the dielectric medium during operations. This depends on several variables, including temperature, ohmic resistance, flow rate, precipitate accumulation, electrode spacing, electrode lengths and coil turn-count ratios. A phase-lock-loop-electronic (PLL) circuit aids in the maintenance of resonance during operations[5–7].

Three replicate resonant cavities were constructed and used to test how this electrolysis technique altered water chemistry and removed metal contaminants. Our goal was to test the behavior of two different dielectric mediums, freshwater (FW) and seawater (SW). The FW samples were sourced from a residential well to test the ability of the QKF to remove trace levels of contaminants in drinking water to evaluate if this technology would be applicable to more contaminated FW systems. Similarly, the SW was sourced from a relatively pristine coastal setting to assess trace level changes in contaminant levels to evaluate if the technology shows promise for deploying in more contaminated settings. Each resonant cavity vessel had two different sets of constructed electrodes: S/S304 (SS) electrode set, and an Aluminum 6061 (Al6061) electrode set to evaluate how electrode composition

[1]Quantum Kinetics Corporation, Arlington, WA, USA. [2]Marine and Coastal Research Laboratory, Pacific Northwest National Laboratory, Sequim, WA, USA. [3]Kent Design and Development, Sequim, WA, USA. ✉email: mckanebuller@gmail.com

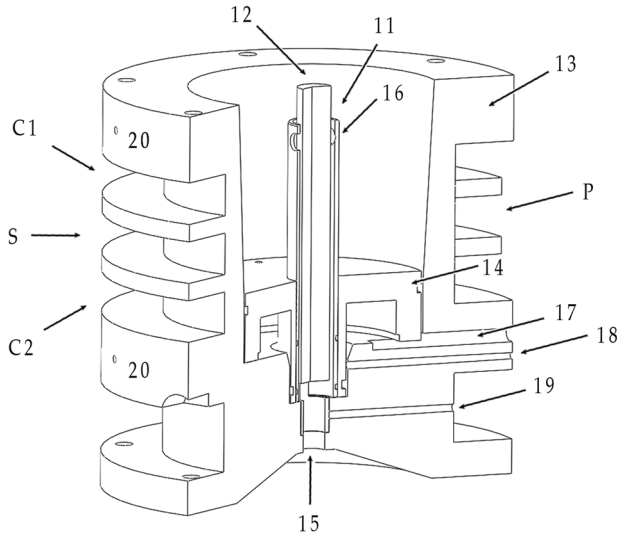

Fig. 1 Quantum Kinetic Fusor design. Coil (C1) and (C2) are respectively Helmholtz coils. Secondary step-up coil (S) laid in conjunction with Primary (P) coil determines resonant voltage to cell. Increasing (S) turn count in reference to (P) turn count increases voltage levels. Transformer tape can be positioned between coils creating an electrical stopgap. (S) and (P) coils positioned between (C1) and (C2) establish a classical Maxwellian Coil arrangement. Modular device can be arranged in series or parallel configuration. Electron Extraction is established between electrodes (20), (12) and (11) respectfully. Transparent acrylic lens (14) allows 660 nm (deep red) photon excitation from LEDs to be passed into resonant cavity and stimulates liberated gaseous matter ions in their quantum orbiting electron jumps (K, L and M shells). (17), (18) and (19) are terminal connections for electrodes and LED photon cluster array. Modular design can be stacked in series or parallel arrangement. Polarized dielectric mediums flow direction is from 15 (enter) to (exit) 16 respectively during operations.

altered water purification performance and/or added dissolved metals sourced from the electrode to the treated sample. For each dielectric or electrode sets we analyzed triplicate source water blanks (SB; i.e., the source water), chamber blanks (CB; i.e., water added to the chambers without voltage applied) and treated samples (T; i.e., voltage applied). Electrolysis parameters are described in Table 1.

A variety of water chemistry measurements were made to evaluate changes in bulk geochemistry, dissolved metals, carbonate speciation, and the stable isotopic composition of the water.

RESULTS

Exotic photon emissions during experiments (Amptek - SiPIN - XR-100CR)

First, we describe photon signatures during the experiments to provide context on the distinct conditions occurring during water treatment. Photon signatures ranging from 1 to 20 KeV were successfully detected during all experiments (Fig. 2). Photon values were taken throughout the experiment at 1 min, 2 min, 6 h, and 8 h. This allowed photon excitation spectrum BLUE shifts to be evaluated if any. Static background radiation values were also taken between each interval to establish if radiation leaked into the dielectric and/or out of device. Background radiation values were consistent with non-radioactive contamination during off states. Radiation signatures did not linger post de-energizing of the device. Radiation signatures were only detected during unipolar pulse train input at resonance.

The (B2) experiment is a radioactive ^{55}Fe calibration sample while (1B), (3B), (4B), (5B) and (6B) are ambient lab background

Table 1. The experiment input characteristics per electrode and dielectric set (bold).

Freshwater Experiment (FW) - Stainless Steel T304	Seawater Experiment (SW) - Stainless Steel T304
Resonance: 5.3KHz (Second Harmonic)	Resonance: 2.9KHz (First Harmonic)
Gate Frequency: 360 Hz	Gate Frequency: 360 Hz
Idle Power: 4.4 watts (Pulsing Circuit)	Idle Power: 6 watts (Pulsing Circuit)
Input Power: 6.3 watts (Pulsing Circuit + Voltage Applied)	Input Power: 7.1 watts (Pulsing Circuit + Voltage Applied)
Power: 1.9 watts	Power: 1.1 watts
Amperage: 0.0475	Amperage: 0.0275
Voltage: 40 v Unipolar Pulsed DC	Voltage: 40 v Unipolar Pulsed DC
Duration: 8 h	Duration: 8 h
Freshwater Experiment (FW) - Aluminum 6061	**Seawater Experiment (SW) - Aluminum 6061**
Resonance: 12KHz (Second Harmonic)	Resonance: 4KHz (First Harmonic)
Gate Frequency: 360 Hz	Gate Frequency: 360 Hz
Idle Power: 2.2 watts (Pulsing Circuit)	Idle Power: 3.4 watts (Pulsing Circuit)
Input Power: 4.1 watts (Pulsing Circuit + Voltage Applied)	Input Power: 5.4 watts (Pulsing Circuit + Voltage Applied)
Power: 1.9 watts	Power: 2.1 watts
Amperage: 0.0475	Amperage: 0.0525
Voltage: 40 v Unipolar Pulsed DC	Voltage: 40 v Unipolar Pulsed DC
Duration: 8 h	Duration: 8 h

Quantum Kinetic Fusor operating characteristics. The experiment inputs characteristic per electrode set and dielectric set. All experiments were conducted for 8 hours. During all experiments a gate frequency of 360 Hz was maintained. Dielectric constant values varied from SW and FW causing different resonant frequencies. First harmonic resonant oscillator modes were used for SW while second harmonic resonant oscillator mode were used for FW. Highest potential harmonic resonant voltages were verified with a Triplett Model 630-PL multi-meter.

radiation levels while device is OFF (Fig. 3b). It appears that the radioactive ^{55}Fe calibration sample has similar overall total emissions as the device while ON (2000–2500 counts). The raw photon data indicates both positive (+) and negative (−) photonic excitation regions. An interesting observation is the resonant ringing that occurs between ON/OFF subsequent 360 hz Gate Unipolar pulse bursts. Detected photon data seems to have characteristics associated with inner atomic electron-capture events and potentially neutron-capture events[8–23], (micro-atomic cavitation). We believe that the photon emissions extend down into the UV A, B and C ranges. However, due to the beryllium lens on Amptek, the effectively attenuated detectable ranges are from 1 to 20 keV.

Changes in electrodes weight pre and post experiments

Next, we describe changes in electrode weights to provide context on how electrode composition influences water chemistry responses to our treatment. Weight measurements were taken of electrodes sets with both S/S304 and Al6061. This was done with pre-test, chamber-blank and treated samples. The S/S304 electrode weights were taken post CB, but not with Al6061. The S/S T304 SW-T cathode recorded a weight increase by an average of 0.125 g while the anode showed an average reduction in weight

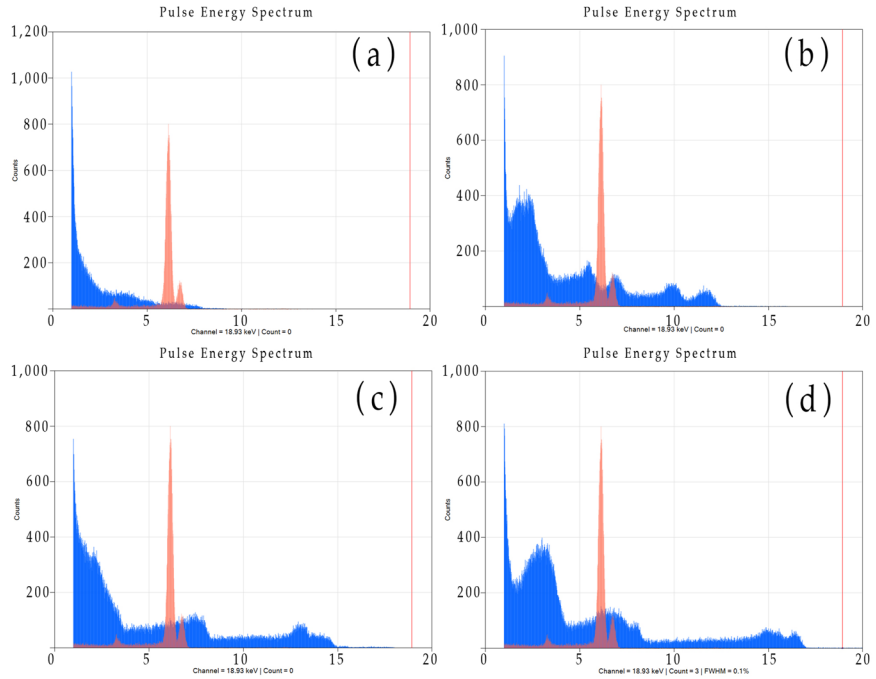

Fig. 2 Blue spectrum is photon emissions during operations. Red spectrum is radioactive ^{55}Fe calibration sample in reference to device. **a** At 1 min shows strong 1 KeV emission lines at start-up with a gradual envelope falloff towards 7.5 KeV[8]. Spectrum **b** after 2 min of operations shows substantial envelope growth in photonic values at 3.5 KeV, 5.7 KeV, 6.1 KeV, 10.2 KeV and 12.5 KeV. Spectrum **c** after 6-h shows an even further widening of the photon emissions with distinct peaks at 1 KeV, 6.6 KeV and 14 KeV shown as dominant. It appears that maximum tapered out emissions were detected approximately between 14 and 17 KeV. Spectrum **d** after eight hours shows the highest maximum emission value at 18.93 KeV (RED vertical line) with strong peaks between 3.55 KeV, 6.3 Kev, 15 Kev and ~18 KeV. RED spectrum on the graphs shows the radioactive ^{55}Fe calibration sample. Note: BLUE Spectrum values (**a**–**d**) are from FW experiments and the S/ST304 electrodes. See Supplemental Fig. 3 for SW experiments.

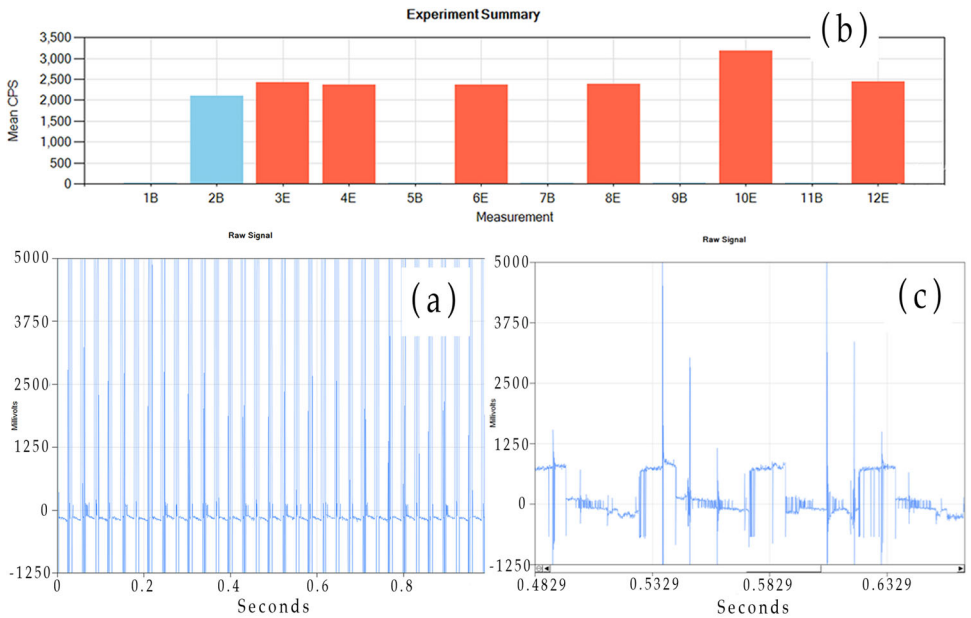

Fig. 3 Photonic energy values throughout the experiment. a The measured photon peaks over 5000 mV. Source data also shows photonic emissions in the negative regions (de-excited state) of the detector, which are consistent with elastic and inelastic Compound Nucleus renormalization[54]. **b** Summary values of the experiments in conjunction with radioactive ^{55}Fe and ambient background data points between run-time internals. **c** Photonic data zoomed in, which detects transient photonic residual ringing spikes. This calibrated photon data shows atomic absorption coefficient behavior during amalgamation as the data crosses the (0 v) plane reference during OFF 360 Hz gate pulses. Note: Spectrum values (**a**–**c**), are from the SW experiments using stainless steel electrodes.

Table 2. Average gain (positive values) or loss (negative values) of electrode mass in grams.

SW-SS	Cathode	Anode	Cathode-2	SW-Al	Cathode	Anode	Cathode-2
Electrode Set #1	0.089	−0.349	0.014	Electrode Set #1	0.007	0.127	−0.007
Electrode Set #2	0.127	−0.578	0.013	Electrode Set #2	0.01	0.058	0.001
Electrode Set #3	0.159	−0.346	0.005	Electrode Set #3	0.006	0.031	0.014
Average	0.125	−0.424	0.0106	Average	0.0076	0.072	0.002

Electrode set average weight change from experiment. The table shows positive number, which is gains, in atomic weight of electrodes. While negative number indicate reduction of electrode weight. Al6061 is a non-transitional metal alloy, which only mildly interacts with electro-static oxidation flux fields. It should be noted: that electrode set "Cathode-2" swings positive (+) to (−) during operations inducing a (0) zero voltage crossing plane within the dielectric within Tri-Coil-Transformer (TCT). The only average weight loss was with anode of S/S304. The only electrode that showed reduction in weight was the SS/304 Anodes. The average weight reduction of the Anode was 0.424 grams over three different experiments.

by 0.424 g. FW-SS experiments showed an average cathode reduction of 0.005 g. Anode average weight reduction was 0.027 g. Al6061 electrode weight changes pre- and post-exposure to FW and SW weight values all increased except for the Cathode-2 from experiment. The average weight increase in SW-Al anodes was 0.99 g. No CB weight values were taken for FW-Al and SW-Al due to apparent redundancies (Table 2).

Precipitate weight values vs. electrode weight lose values

Accumulation of sediments is described here to provide context on the processes driving removal of dissolved metals. Post treatment FW-SS samples visually showed light-brown and yellow sedimentation, while SW-SS showed dark brown, green, and black sedimentation. Precipitates were collected from all experiments by centrifugation of treated water.

When averaging the three FW-SS experiments, there was a net average loss when compared to the other experiments' averages. The FW-SS experiment showed an average net weight loss of 0.0238 g over 8 hours, while SW-SS experiment showed an average weight net gain of 1.50 g. The Al6061 experiment with SW showed the largest average net gain of 1.98 g (See Fig. 4). This is consistent with prior art understanding of Al6061 as a non-transitional low redox reacting metal alloy which does not show degradation during low current density (<1 A cm^{-2}) electrical stimulation i.e., anode pitting/cracking.

Current density of electrodes, overall operational readings & smart Geiger (uS/h) Readings

The current density of the electrodes during operation is reported in order to compare the energy efficiency of this water purification approach with the current state of the art. The total current was 0.04275 A at 40 v input, which converts to 1.9 W of power. The total electro-statically active surface area of the electrodes is approximately 300 cm^2 +/−5 cm^2. The total current density per surface area is 0.142 mA cm^{-2}. The current density is 126.5% lower than current electro-coagulation water purification applications[24]. During experimental operations the magnetic field lines fluctuated with a swing between ~100 and 300 mG - (Tri-Field Meter − 100XE). The fluxing magnetic field was induced by a constant 360 Hz-Gate frequency. Magnetic field detector was placed ~15 cm from the operating QKF device. DC electric voltage was monitored to the electrode's anode and cathode (~3–4 V) was recorded. Once the Triplett 630-PL multi-meter selector was switched over to AC detection mode, there was a biased AC electrical voltage between the anode and Cathode-2 during operation. No AC voltage was detected between anode and cathode, just between anode and Cathode-2. Temperature of the device stayed relatively consistent (0.5 °C) with ambient environment. The temperature of the dielectric post treatment i.e., 8 h exposure was only 0.8 to 1.1 °C warmer that the outside surface of the apparatus. Smart Geiger detector was able to detect a reading of ~370 *u*Sv h^{-1} during a 60-s exposure to operational device. The Smart Geiger was placed 5–10 cm away from operating core of device (Fig. 5). The Smart Geiger detector device was calibrated using ^{55}Fe and ^{137}Cs before and after operational use in experiments. See Supplemental Fig. 4 for calibration of Smart Geiger.

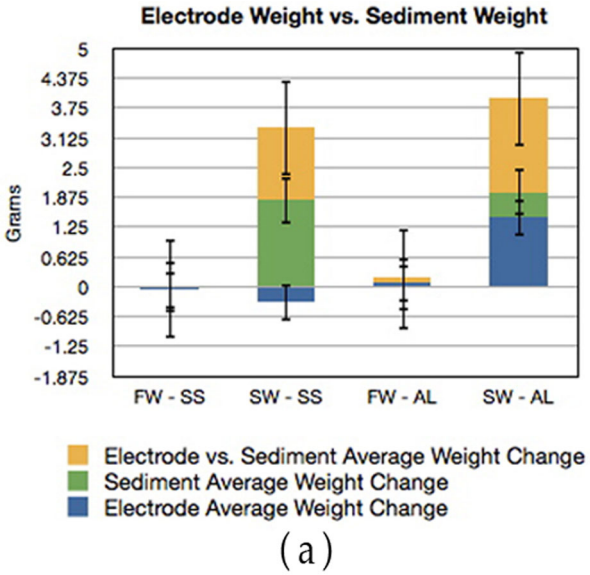

Fig. 4 Electrode and sediment mass gain and loss. The only experiment that showed net average loss was FW-SS, but the amount lost was negligible. The largest sediment collected was 2.68 g, which was collected from SW-SS experiment set #1. A larger sedimentation average weight gain was established with Al6061 electrodes. Trace amounts of Ag were detected on all electrodes surfaces post experiment with Al electrodes. Error bars denote ± 1 standard deviation.

Atomic isotopic composition & dissolved metal and ion concentration changes

Due to the photon radiation detection previously described, we decided to investigate the isotope values of water pre and post treatment. The values investigated were $d^{18}O$, dD, and ^3H (Fig. 6). In the natural environment, temperature is the primary control on the isotopic composition of precipitation. With increasing temperature, precipitation becomes enriched in the heavier isotopes, $d^{18}O$ and dD, in a linear relationship. It is also known that not only temperature, but also solar wind flux intensities are associated with cosmic radiation influences, which change aquatic $d^{18}O$, dD and temperature values. The temperature of solar wind characteristics in the North and South Pole regions vs. equator regions determines $d^{18}O$ and dD signatures.

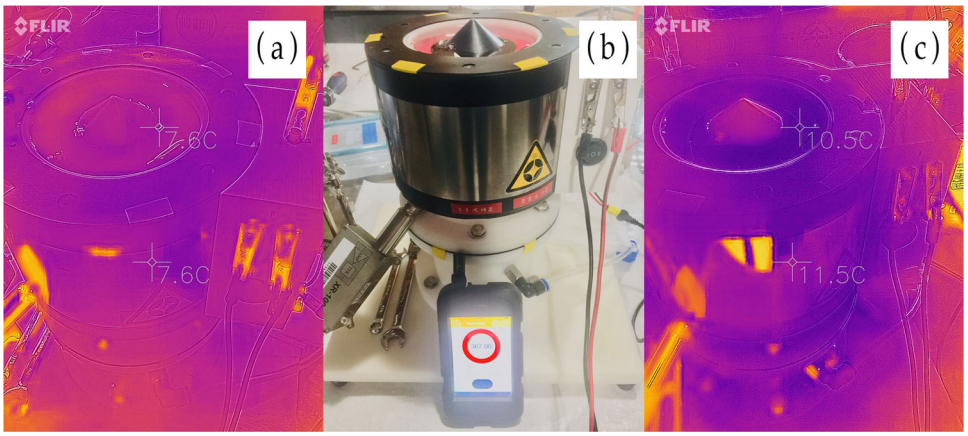

Fig. 5 Temperature and Geiger counter signatures of device before and after energizing. The three images are from one of the FW-AL experiments. **a** Shows the FLIR temperature signature of device before energizing FW-AL experiment 7/23/2021 at 5:56am. **b** Shows the Smart Geiger counter next to device detecting 367 uS h^{-1} within 60 s of exposure to operational device. **c** Shows FLIR temperature readings 3 h into experiment. The temperature of dielectric value was 10.5 C while the vessel was 11.5 °C. The final temperature reading after 8 h was 15.3 °C to dielectric and 15.8 °C to vessel. The device and dielectric steady increased in temperature in accordance with the ambient air within the lab.

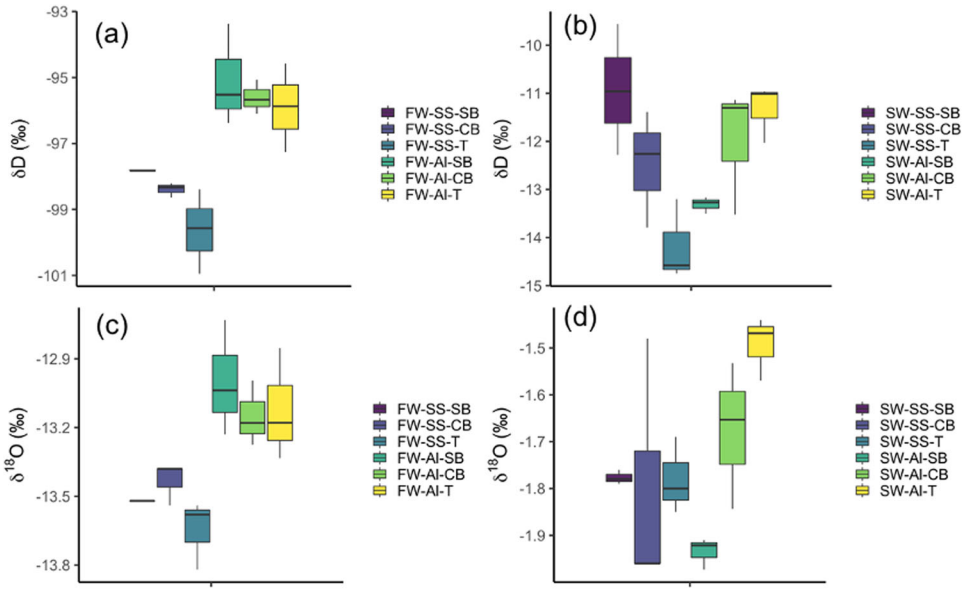

Fig. 6 Water stable isotope changes following water treatment. dD values in the **a** FW and **b** SW experiments and $d^{18}O$ values in the **c** FW and **d** SW experiments with stainless steel (SS) and aluminum (Al) electrodes. SW experiments show diverging patterns of dD and $d^{18}O$ between SS and Al electrodes. Data suggests the isotope manipulation occurs during OFF modes with CB. The box and whisker plots denote the median value (line within each box), upper and lower quartiles (top and bottom of box), and minimum and maximum values (whiskers).

There was a steady decrease in heavy isotopes of $d^{18}O$, dD and even ^{3}H post treatment. Isotopic readjustments are observable in the CB and as well as treated samples. This is also supported by a steady linear increase in pH (decreased value present of H + ions) values of water during CB and Treated water dielectrics.

FW-SS treated $d^{18}O$ values dropped from −13.5‰ in the source blank to −13.8‰ while dD values dropped from −97‰ in the source blank to −100‰ in the treated samples (Fig. 6). ^{3}H showed reduction in FW-SS values of 0.58 TU to 0.53 TU. Standard deviation for Tritium Enrichment Electrolytic (TEE) is 0.25 TU. In this test, average ^{3}H value fell by approximately 9% within just 8 hours of treatment. That is over 1% per hour of exposure to a current density of 0.142 mA/cm^{-2} or 1.9 watts of power. This observation is not statistically significant, however it is an observable trend that warrants further investigation due its initial small concentration value. As described previously, photon energizes average value was ~5.7 KeV while the maximum value reached was 18.4 KeV for the FW-SS experiment. This photon excitation level of this nature (1–20 KeV) is associated with ^{3}H to Helium beta-decay events[24–34]. SW-SS $d^{18}O$ values showed little change. SW-SS dD values steadily decreased from −11‰ in the source blank to −12.5‰ in the chamber blank, and −14.7‰ in the treated samples. Overall trending of isotopic changes show that SS and Al electrodes reduce heavy isotopes of dD and d18O, except for the exception of SW-Al dielectric. The isotopes tend to increase dramatically with SW-Al experiments. CB has an influence on the isotopic values as well.

Changes in dissolved metal concentrations seem to be supported by the isotopic characteristic transformations in addition to photonic excitations observed. A decrease in As, Ba, and Cu were observed in FW-SS treated samples. No significant changes were observed in Cd levels, which were below the detection limit in all but one FW-SS experiments.

Table 3. Change in metal concentrations (μg L^{-1}) following treatment measured by ICP-OES.

Treatment	Al	Ba	Ca	Cr	Fe	K	Mg	Mn	Na	Ni	Sr
FW-SS	NA	−1.17	−2699	2100	38.6	−76.4	−1539	0.777	−56.7	212	−16.4
SW-SS	NA	−2.03	−290	64.7	12950	3643	−44633	3387	8100	10581	−50.5
FW-Al	405	−1.32	−2203	0.424	−1.36	−27.0	−2046	1.50	−20.0	0.334	−16.7
SW-Al	781	0.515	−8200	0	1.30	7167	−44333	70.5	110000	0	−37.7

Changes in metal concentration of dielectric post experiment. Average change in metal concentration of elements pre (i.e., source blank) to post experiment (i.e., treated) values determined via ICP-OES. Positive number present gains in material and negative numbers are reduction values.

Table 4. Change in metal concentrations (μg L^{-1}) following treatment measured by ICP-MS.

Treatment	Ag	As	Cd	Cu	Pb	Se	Zn
FW-SS	0.150	−1.21	−0.003	−15	0.004	0.044	5.42
SW-SS	NA	NA	0.091	452	0.015	NA	9.19
FW-Al	0	−0.875	0	−163	0.009	−0.045	−3.47
SW-Al	NA	NA	0.020	−1.01	0.127	NA	3.08

Average changes in concentration following treatment. Average change in metal concentration of elements pre (i.e., source blank) to post experiment (i.e., treated) values determined via ICP-MS. Positive numbers represent gains in material and negative numbers are reduction values.

Pb and Al substantially increased in the chamber blanks for both SW and FW experiments with SS electrodes but did not increase in the treated samples. It is likely that the chamber blanks had these metals leached into the water, which the treatments subsequently removed. This may also be further evidence to support the notion that external E.M.F. (radio, microwave and cell phone towers) simulation to the apparatus influences dielectric renormalization. This increase within the CB was also observed with SW and FW in Zn values. More study is required to determine the exact reasons are for this phenomenon.

Cu had divergent patterns in FW and SW experiments, decreasing in FW-SS and increasing in SW-SS. Cu levels increased in the chamber blank during the 8-hour soak with SW-SS. Ni values increased in FW-SS by 212–239 μg L^{-1} (Tables 3–4). In addition, Ni in the SW-SS experiment increased by 10,581 μg L^{-1}, which is likely related to electrode pitting, whereas Ni only marginally increased in the FW-Al experiment by 0.334 μg L^{-1}. In the SW-Al experiment the values of Ni were too low to detect.

K concentrations were elevated only SW experiments, whereas slight decreases were observed in the FW experiments. SW-SS experienced an increase in potassium levels by 3643 μg L^{-1} and SW-Al detected an increase of 7167 μg L^{-1}. Salinity was reduced by 1.8% in SW-Al while SW-SS dropped by 3%, perhaps related to the large decrease in observed dissolved Mg concentrations (Table 3). The reduction of salinity and the increase of potassium are, potentially, due to a transmutation metabolic ATP cycling i.e. [Na + O + H^+ = P] byproduct. This suggests a type of synthetic stimulated photosynthetic process[35]. See Table 3, Supplemental Figs. 5 and 6. Ca values decreased in all experiments and Ca ions were collected/observed on the cathode post experiments for both Al and SS electrodes. FW-SS showed a slight increase in Ag. Very slight increases in Se were observed in the FW-SS treated samples compared to a slight decrease in the treated FW-Al samples. It should be noted that Ag, Ca and Cl was detected on all Al electrode surfaces post experiment. We observed arsenic reduction of 93.7% and strontium reduction of 13% in the FW-SS experiment.

Post experiments of FW-Al, we observed and collected paramagnetic sedimentation from electrodes to be composed of trace elements comprising of Re, Yb, Sn, Ag, Nb, Zr, Ni, Br, Zn, Ni, Fe, Ti, V, Cr, In, Si, Pb, and S. C saturation values of paramagnetic sediment was between 88.6 and 12.8%[36–40]. A titanium-vanadium nano-sphere was also detected in the paramagnetic sedimentation post experiment with FW-Al (Fig. 7a).

Changes in Water pH Levels

For FW samples, we observed a steady increase in pH values throughout the experiments with both SS and Al electrodes (Fig. 8). On the other hand, a drop in pH was detected when SW dielectric was energized. This occurred with both SS and Al electrodes in SW. The pH elevation during FW experiments is expressed as H + ions either off gassed as hydrogen from the resonant cavity or some other ionic exchange or atomic reaction or FW carbonate buffering destabilizations. Regardless, SW pH significantly acidifies, which shifts the carbonate system towards CO_2. More study is necessary to confirm the potential of biosphere purification applications of the QKF device. Data does suggest that, at some level, biological index stimulation values increase post treatment. CDOM (non-filterable organic matter), BIX, humic matter, fluorescence, and cyanobacteria values increased in both Al and SS with SW experiment. See Supplemental Figs. 5 and 6.

SW water samples for both electrode types showed complete removal of calculated CO_3 values with HCO_3 values dropping by approximately 50%. Calcite ($CaCO_3$) was deposited on cathode and Cathode-2 of the electrodes set in all Al experiments. See Supplementary Fig. 10. Calculated CO_2 values increased accordingly during SW experiments with both the SS and Al electrodes.

The device increases pH levels of SW and FW. This is further evidence of free H + ions interacting via isotopic re-arrangement within the device. This apparatus can be used to renormalize pH levels of rivers, ground water, and even ocean water. Evidence suggests that pH levels rise even during CB experiments with SW-SS (no power and not connected to electrical mains).

DISCUSSION

The electro-transmutation (ET) device described here shows promise in industries associated with isotopic water purification, energy harvesting, element transmutation, and in radioactive wastewater treatment. Results indicate that utilization of the resonant magnetic fields focused in conjunction with electrostatic temporal flux lines aid in dissociation of water, both FW and SW, with no electrolyte present. Current density levels are unprecedentedly low (0.142 mA cm^{-2}) as compared to prior art technologies in these sectors, even cell membrane devices[41]. It is open for discussion that this might be a synthetically driven mechanical hydrostatic carbon burning process (synthetic gravity). This postulation is driven by the increase in carbon, silver, sodium, magnesium, titanium, lead, and oxygen present upon dried electrodes. SEM values detect nanostructures associated with metal hydrides including a hyper magnetic meteorite characteristic-like black rock post treatment. However, more study is necessary to confirm these findings.

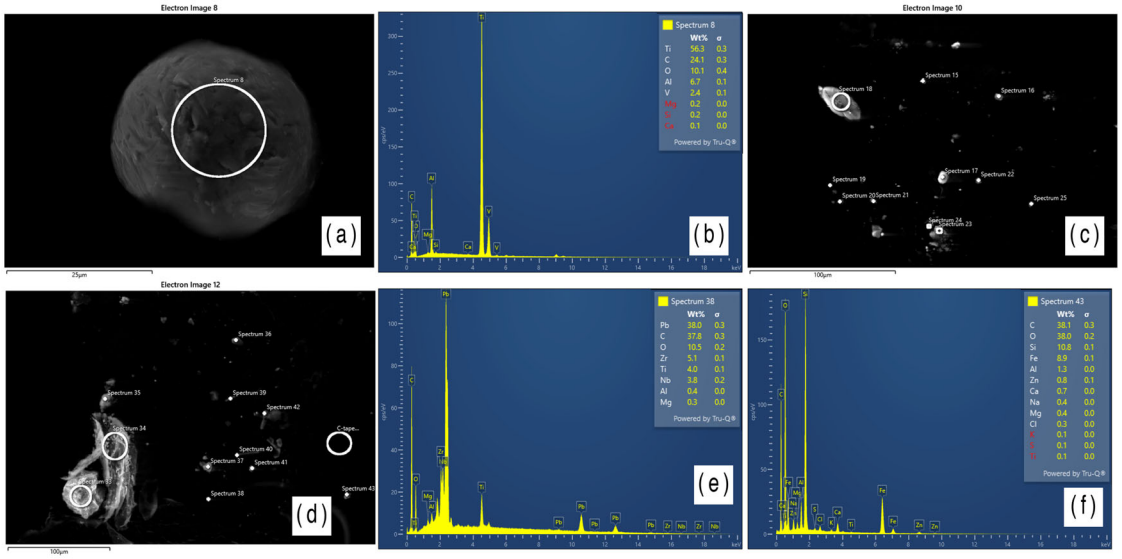

Fig. 7 SEM and EDS values post-treatment for the FW-Al experiment paramagnetic sediment. a Shows the nano-sphere of titanium-vanadium **b** is the EDS spectrum of the nano-sphere. **c** Is the overview SEM image of sediment on carbon tray **d** is the overview SEM image of sediment group 2 on the carbon try. **e** Shows the spectrum analysis of specimen 34 (**f**) while depicts the spectrum analysis of specimen 43.

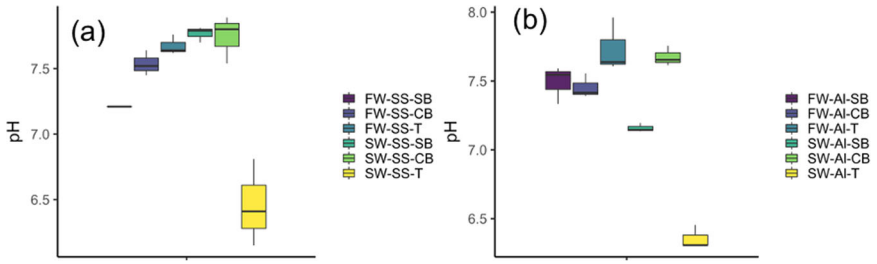

Fig. 8 Shifts in pH following treatment. pH values of experiments with FW and SW with two different electrode compositions i.e., SS and Al. **a** Depicts the FW and SW samples treated with stainless steel electrodes. **b** Depicts the FW and SW samples treated with aluminum electrodes. The box and whisker plots denote the median value (line within each box), upper and lower quartiles (top and bottom of box), and minimum and maximum values (whiskers).

The resonant electro-transmutation process is most likely caused by electrode intra-band electron transitions interacting with the dielectric medium's free electron intra-band known as space-charge polarization. A free particle may absorb/emit a photon, thereby remaining free. This means, the field interacts only with the scattering part of the one-particle spectrum. In solids, this corresponds to intra-band transitions. Absorption of a photon also leads to excitation of a bound particle into the continuum, i.e. to photo-ionization, (or to recombination in case of emission of a photon) Finally, Absorption/emission of a photon leads to transitions of a particle in the discrete part of the spectrum, from one level (band) to another[42]. The resonance electro-transmutation Space-Charge Polarization induces emission/absorption of photons to become trapped and/or exchange intra-bands electron transitions i.e., transmutation between solids (electrodes) and interfacing liquids (dielectric mediums). This would be classified as a Quantum Thermodynamic reaction.

Radiation signatures associated with these values are typically signatures associated with tritium to helium-3 β^-/β^+ elastic scattering, solar winds (1 KeV), carbon ion flux (12 KeV), and inelastic scattering interactions (x-process: cosmic-ray-spallation i.e. 5.66 KeV). It should be noted that, "stellar cores possess high enough temperatures for the thermal excitation of low-energy nuclear levels of magnetic type (~1 KeV scale), which could emit axions during the de-excitation (g-an coupling)". These research findings suggest that element fusion is being produced in the resonant cavity. After all, particle accelerators, which fuse light elements together, share similar soft x-ray emissions within cyclotrons and synchrotron[43] during atomic syntheses procedures.

This is suggestive of positron atomic tritium ± beta-decay events. Rare, morphological heavy metallic, were detected post treatment indicating an atomic or low energy yield nuclear event is occurring inside the resonant cavity. The ET products and byproducts have shown to be a variety product including and not limited to: hydrogen powered propulsion engines/rockets, carbon sequestering, carbonaceous chondrite magnetite formation, pollution treatment, nano-oxide shapes including spheroids, hexagons, cubes and quasi-crystals; wastewater remediation, simulation of 4th phase of water[44], magneto-tactic bacteria enlargement, nano-sphere magnetite technology for stealth coatings (RAM), phytoplankton stimulation, hydrides, radioactive tritium harvesting/purification and more. See Supplemental Figs. 7 and 8. Prior to these SW and FW test experiments, the resonant cavities devices were tested with a CO_2 gas injection (3–5 psi) with distilled water as the dielectric between electrodes. Transparent paramagnetic crystallization of CO_2 graphite morphologies was discovered post treatment[45]. See Supplemental Fig. 9.

The range of technological applications of this system is only limited by the human imagination. Again, more testing and research are required to confirm and re-confirm these findings and discoveries. Additional research should be focused on deuterium oxide dielectric mediums.

This research suggests that the illusive Zitterbewegung wobbling architecture of the electron can be tapped into

mechanically through ET effects (nano-technology electron cavitation events – negative differential electron pressures). As such, it may be a viable alternative to the star building fusion device(s) currently in development around the world[46], that rely on the violent smashing together of atoms at extreme velocities and at temperatures potentially too intense to control safely and efficiently. Rather, the ET method proposed here entails a naturally gentle approach to electron transmutation by relying upon low temperature, low energy inputs simulating nature's own transformation schemes. This approach may provide a basis for greater optimism for a clean and abundant energy future, as well as an alternative method for water isotopic purification on a universal scale[47–49].

Here we demonstrate one potential application for the resonant electro-transmutation (ET) process in a heterodyne stance with the Quantum Kinetic Well™. Based on a series of experiments we demonstrate that the ET process can effectively influence changes in the isotopic composition of both freshwater and seawater. Likewise, the process removed a variety of contaminants such as arsenic from water. These outcomes are accomplished using an unprecedentedly low current density value of 0.142 mA cm^{-2}. Thus, the technology shows promise for being an efficient means for purifying water for a variety of purposes. Future research should examine how the ET process modifies the chemistry of water with diverse chemistries. For example, we observed purification of relatively pristine water sources, effectively removing trace levels of certain elements. A key question remains as to how this process functions as contaminant levels increase and likewise how scalable is the technology to handle large quantities of water? Finally, these preliminary findings suggest that in addition to showing promise for water purification applications, the ET process may be applicable to a variety of other industrial applications, including stand-alone, pristine energy generation systems, which should be explored in the future studies.

METHODS

Quantum kinetic fusor device

The QKF™ device is a modular designed resonant cavity machined out of polyoxymethylene Delrin (Acetal) material (Fig. 1; 13) (Interstate Plastics). The device is 6-inches in diameter and 6-inches tall. Externally, the design houses the tri-coil resonant coils, while internally seated two (anode 11 & cathode 12) electrodes in a proportional linear stance. Delrin (Acetal) 13 acts as an insulating material and a stable neutron moderator during operations. The tri-coils (C1, C2, and S) are composed of either magnetic copper wire (TEMCo Industrial LLC) or resistive stainless steel wire (SANDVIK – Alloy Kanthal A-1) coil wrapped around the external cavities of the modular Delrin housing. A Helmholtz or Maxwell coil (S, P, C1, and C2) stance can be arranged around the electro-conductive electrodes 12, 11, and 20, which is typical Stainless Steel T304 (Fig. 1). Many other electrode materials may be used to form unique oxide nanostructures. Acrylic lens 14 holds a fabricated LED cluster array (30 × 5 mm LEDs) concentrically beneath the electrodes 11, 12, and 20 respectfully. LED cluster array is pulsed in sync with primary coil P unipolar pulse bursts into the QKF™. This effect enhances and causes inner atomic emission/absorption of the electron of the hydrogen atoms to further promote dissociation of dielectric medium such as water. This also aids in targeting not just liquids, solids but also gaseous matter targets[50,51].

The positive electrode, i.e., anode is constructed from a seamless S/S - T304 seamless tube with an outer diameter of 1.9 cm that is 10.1 cm long (Shanghai Baoluo Stainless Steel Tube Co., LTF). The negative electrode, i.e., cathode is 1.3 cm diameter round bar stock S/S - T304 with a length of 12.7 cm. Longitudinal gap spacing between electrodes is ~0.16 cm. A second cathode tubular 2.5 cm outer diameter electrode is placed on the outside of the anode with a gap spacing of ~0.32 cm. This electrode is referred to as Cathode-2 electrode. The QKF's current density is 0.142 mA cm^{-2} (i.e., total electrode surface area of 300.09 cm^2). A Delrin cap is placed over the electrodes to limit electrostatic charge leakage throughout the dielectric medium. The non-conducting Delrin cap also aids in buoyancy trapping of dissociated (ionized) gaseous matter from liquid dielectrics such as protium, deuterium, tritium, oxygen-16, nitrogen, neon, argon and oxygen-18 for a secondary electrode exposure i.e. recycling exposure effect[52]. This allows for an atomic-recycling effect; in which liberated gaseous matter is re-exposed to electrically energize electrostatic and magnetic field lines. See Supplemental Fig. 1.

Operational resonant frequencies can vary from 1 Khz to 1 Mhz depending on the coil turn counts, waveguide size-length ratios and the cavity's coil ohmic values.

This apparatus utilizes electrical phenomenon including electron spin rate disturbances, Electrostatic/Magnetic Bremsstrahlung, Zitterbewegung 11, Stark effect, Auger effect, Zeeman effect, Quantum Tunneling and Hall effects, Electron Bifurcation Destabilization 12, Compound Nucleus, Elastic, and Inelastic atomic electron scattering. The physical force of the electrons within the "closed-loop" resistive, inductive capacitive tri-coil transformer (T.C.T.) circuit utilizes a low power on-demand approach to dissociate dielectric medium(s) of liquid, air, and metallic liquids.

In addition to the unipolar inputs to the device, a new form of electrical input is also superimposed (heterodyne mixing) onto/into the voltage zones (Radiotron). This negative differential electron pressure relies on The Quantum Kinetic Well™ (USPTO# 11,233,421 - track-one status, issued 1/25/2022) 13. See Supplemental Fig. 2. The resonant electrostatic force(s), during operations, manufacture a fluxing perpendicular bisector uniform magnetic field superimposed onto the electrodes surface (free electrons) by the resonating tri-coil transformer (TCT) wires during operations. Dielectric electron cloud bifurcation matrices are agitated and ultimately plucked (i.e., micro-cavitated) at the quantum level by electric and magnetic field lines (Poynting Vectors) directly into the dielectric within a resonant closed-loop TCT circuit. The fluxing field lines create a Fluxing-Capacitor effect between the two excited electrodes. This physical phenomenon promotes radioactive atomic destabilization/renormalization E.M.F. work to be done with little to zero amperage in flux from the pulsing power supply. This can be referred to as photodisintegration radiation or dielectric cavitations, which are induced from resonant standing wave motion, not by ground-state electric current i.e., amperage, but from cavitating negative differential electron transient pressure of the dielectric substance.

Simply attenuate the power supply voltage (Powerstat Variable Autotransformer - Type 21) to enhance the probability of the temporal polarization perturbations i.e., electron-capture (dielectric cavitation) events. This process can be classified as a mechanical electro-physical Electron-Pump or Electrostatic Venturi. For further details of operations please refer to submitted utility patent documents 20210156037 - USPTO. See Table 1 for electrolysis parameters.

Experimental design

Electrolysis experiments were run in triplicate with freshwater collected from a residential well in western Washington state, USA, representing a potable water source, and seawater collected from Sequim Bay in western Washington state, USA, representing a relatively pristine marine setting with limited human-derived pollution. Well water was filled from a residential tap. The seawater was collected from the Pacific Northwest National Laboratory's seawater intake located at the bottom of Sequim Bay. The fresh and saline source waters were collected in 10 L carboys that were soaked in MilliQ water for 24 h, rinsed with MilliQ, and again rinsed with the source water prior to collection. Electrode sets were soaked in nitric acid for 1 h followed by MilliQ water soak for 24 h pre-experiment run. For each experiment, a source water blank, was collected in which water from the carboy was directly placed into bottles for analytical measurements. This served as an indicator for pre-treatment water chemistry. A chamber blank was also collected for each experimental replicate, whereby the source water was soaked in the experimental chamber for an equivalent period as the electrolysis experiment (8 hours) with no voltage applied to the electrodes to evaluate any chemical changes related to exposure to the chamber materials. Finally, electrolysis experiments were conducted for 8 h.

A 500 mL amber HDPE bottle soaked and rinsed with MilliQ water was used for measurements of the stable isotopic composition of water (i.e., dD and $d^{18}O$), pH, alkalinity (and associated calculations of carbonate speciation) and conductivity (and associated calculations of salinity). A 250 mL Teflon bottle, pre-cleaned in hot concentrated nitric acid (85 °C) and rinsed with deionized water, was used for dissolved metal samples. The following abbreviations are used throughout this manuscript to refer to each experimental sample: FW-SB = Freshwater Source Blank; FW-CB = Freshwater Chamber Blank; FW-T = Freshwater Treated Sample; SW-SB = Seawater Source Blank; SW-CB = Seawater Chamber Blank;

SW-T = Seawater Treated Sample. Additionally, the qualifiers SS and AL indicate experiments performed with stainless steel and aluminum electrodes, respectively.

Analytical methods

Prior to removing solids from the samples, freshwater samples were analyzed for pH and electrical conductivity using an Oakton PCTSTestr 50 meter. For seawater samples, pH, Alkalinity, and conductivity were measured using a Mettler Toledo T7 auto titrator. Seawater conductivity was converted to salinity in practical salinity units (PSU). Carbonate speciation was calculated based on the pH and alkalinity data using CO2sys software[53].

Samples collected in the amber HDPE bottles were filtered with GF/F filters (nominal pore size of 0.7 µm) for isotopic analyses. A portion of the filtrate was added to combusted 40 mL amber glass vials for analysis of water stable isotopic composition using a Los Gatos Research Liquid Water Isotope Analyzer. These samples were also analyzed for dissolved organic carbon (DOC) concentrations using a Shimadzu Total Carbon Analyzer.

Samples collected in the Teflon bottles were centrifuged in nitric acid cleaned 50 mL centrifuge tubes and the liquid fraction was decanted into clean tubes and acidified to 1% nitric acid for preservation and metals analyses. The solids were dried at 80 °C for 24 h and weighed. The liquid samples were analyzed for major ions and trace metals via ICP-OES (Perkin Elmer Optima 7300) and ICP-MS (Thermo Elemental iCAP Q with SeaFast sample introduction system).

To evaluate the operating conditions of the device and potential mechanisms underlying the observed water chemistry changes during the experiments, an Amptek SiPIN - XR-100CR detector was used to detect photon signatures ranging from 1 KeV to 20 KeV. The XR-100CR was placed 2–5 cm away from the device at a ~45° angle upwards towards the device's under-belly. Before each experimental session, the XR-100CR was calibrated with a 60-s exposure to a small sample of radioactive ^{55}Fe and checked with background radiation values. The radioactive ^{55}Fe spectrum calibration can be seen in Fig. 2 as the red spectrum peak at 6.2 KeV. In addition to the XR-100CR detector, the Enshey Smart Geiger Counter Nuclear Radiation Dosimeter was calibrated before and after experiments with an exposure of 60 s to samples of ^{55}Fe and ^{137}Cs. See Supplemental Fig. 4.

Post experiment, electrodes were rinsed with MilliQ water and gently scrubbed with sterilized gloves to remove sediment. Electrode sediment was dried for 24 h in a cell strainer 40 *um* micro-filter. Dried sediment and rinsed electrodes were then analyzed with Electron-Dispersive X-Ray Spectroscopy (EDS) (Oxford X-max80) and Scanning Electron Microscope SEM (Apreo VP—Thermofisher Scientific). The University of Washington's Molecular Analytics Facility SEM evaluated dried sediment from post treatments and electrode analysis. Sediment and electrodes weight measurements were conducted with a lab grade LEADzM Electronic Scale: model #B073CFGSZL with a tolerance of 0.002±.

DATA AVAILABILITY

All applicable data is provided in the figures and tables of the manuscript.

CODE AVAILABILITY

Not applicable

Received: 8 March 2022; Accepted: 15 July 2022;
Published online: 11 August 2022

REFERENCES

1. Tong, W. et al. Electrolysis of low-grade and saline surface water. *Nat. Energy* **5**, 367–377 (2020).
2. Kamran, U. & Park, S.-J. MnO_2-decorated biochar composites of coconut shell and rise husk: an efficient lithium ion adsorption-desorption performance in aqueous media. *Chemosphere* **260**, 260 (2020).
3. Yuly, J. L., Zhang, P., Lubner, C. E., Peters, J. W., & Beratan, D. N. Universal free-energy landscape produces efficient and reversible electron bifurcation. *Proc. Natl Acad. Sci. USA*. https://www.pnas.org/doi/abs/10.1073/pnas.2010815117 (2020).
4. Bockris, J. O.'M., Sundaresan, R., Minevski, Z., Letts, D. Triggering of heat and sub-surface changes in Pd-D systems. Department of Chemistry Texas A&M University, 1–15 (1993).
5. Matsuta, S. Electron-spin-resonance study of the reaction of electrolytic solutions on the positive electrode for lithium-ion secondary batteries. *J. Electrochem. Soc.* **148**, 148 (2000).
6. Heising, R. A. The Audion oscillator. *J. Am. Inst. Electr. Eng.* **39**, 365–376 (1920).
7. Sell, J. K., Niedermayer, A. O. & Jakoby, B. A digital PLL circuit for resonator sensors. *Sens. Actuators A: Phys.* **172**, 69–74 (2011).
8. Abdurashitov, J. N. et al. First measurements in search for keV sterile neutrino in tritium beta-decay in the Troitsk nu-mass experiment. *Jetp Lett.* **105**, 753–757 (2017). 2015.
9. Conlon, J. P. & David Marsh, M. C. Excess astrophysical photons from a 0.1–1 keV cosmic axion background. *Phys. Rev. Lett.* **111**, 151301 (2013).
10. Stella, L. Iron K-shell lines from relativistic accretion disks. *EXOSAT Observatory Astrophsyics*. **1**, 19–23 (2021).
11. Roederer, I. U. Neutron-capture nucleosynthesis in the first stars. *Astrophysical J.* **784**, 1–24 (2014).
12. Mouedhen, G., Feki, M., De Petris, M. & Ayedi, H. F. Behavior of aluminum electrodes in electrocoagulation process. *J. Hazard Mater.* **150**, 125–133 (2007).
13. Hansen, C. J. In Quest of the Cosmic Origins of Silver: Silver and gold materialized in different stellar explosions. *Science Daily* (2012).
14. Ouyed, R. & Leahy, D. Spallation model for the titantium-rich supernova remnant Cassiopeia A. *Phys. Rev. Lett.* **107**, 151103 (2011).
15. Gray, L. J. & Beer, J. Solar Influences on Climate. Wiley & AGU. 11–25 (2010).
16. Kalbfleisch, G. R. Limit on Heavy Neutrino in Tritium Beta Decay. Department of Physics and Astronomy, University of Oklahoma, Norman, OK 73019, USA (1992).
17. Takahashi, A. Experimental Study on Correlation between Excess Heat and Nuclear Products by D2O/Pd Electrolysis. Cold Fusion, Heavy Water Electrolysis, Excess Heat, Nuclear Product, Correlation, Helium, X-ray. 1998 年 6 巻 1 号. 4–13
18. Classen, J., Su, C.-K., Mohazzab, M. & Maris, H. J. Electrons and cavitation in liquid helium. *Phys. Rev. B* **57**, 3000 (1997).
19. Porter, F. T. Beta decay energy of tritium. *Phys. Rev.* **115**, 450 (1959).
20. Micklich, B. J. & Jassby, D. L. Implications of polarized deuterium-tritium plasmas for toroidal fusion reactors. 162–168 (2017).
21. Frontera, F. The cosmic X-ray background and the population of the most heavily obscured AGNs. *Astrophysical J., ApJ* **666**, 86–95 (2007).
22. Korchak, A. A. On the origin of solar flare X-rays. *Sol. Phys.* **18**, 284–304 (1971).
23. Hummel, J. A. The first stars: formation under X-ray feedback. *R. Astronom. Soc.* **453**, 4136–4147 (2014).
24. El-Masry, M. H., Sadek, O. M. & Mekhemer, W. K. Mekhemer. Purification of raw surface water using electro-coagulation Method. SpringerLink. **158**, 373–385 (2003).
25. Arnoldy, R. L. Pc 1 Waves and associated unstable distributions of magnetospheric proton observed during a solar wind pressure pulse. *J. Geophys. Res.: Space Phys.* **110**, https://agupubs.onlinelibrary.wiley.com/doi/full/10.1029/2005JA011041 (2005).
26. Lodders, K. Titanium and vanadium chemistry in low-mass dwarf stars. *Am. Astronom. Soc.* **577** (2002).
27. Nittler, L. R. Aluminum-, calcium- and titanium-rich oxide stardust in ordinary chondrite meteorites. *Am. Astronom. Soc.* **682**, (2008).
28. Wainwright, M. Biological entities isolated from two stratosphere launches-continued evidence for a space origin. ResearchGate & Astrobiology & Outreach. 4–5 (2015).
29. Wang, X. Magnetotactic bacteria: characteristics and environmental applications. *Front. Environ. Sci. Eng.* **14**, 56 (2020).
30. Hicks, L. J. Magnetite in Comet Wild 2: Evidence for Parent Body Aqueous Alteration (2017).
31. Friedmann, E. I. Chains of magnetite crystals in the meteorite ALH84001: evidence of biological origin. *Proc. Natl Acad. Sci. USA*. 2176–2180 (2001).
32. GeoLabs. 050721MCLE1. Suspected meteorite identification. Order# 1298 (2021).
33. Hornbogen, E. & Minuth, E. Cracks in metallic meteorites. *J. Mater. Sci.* **16**, 515–522 (1981).
34. Van de Moortele, B. Shock induced metallic iron nanoparticles in olivine-rich martian meteorites. *Earth Planet. Sci. Lett.* 37–49 (2007).
35. Raven, J. A. Origin of the roles of potassium in biology. Division of Plant Science. *BioEssays Wiley Online J.* (2020).
36. Mason, B. Origin of chrondules and chondritic meteorites. *Nature* **186**, 230–231 (1960).
37. Scott, E. R. D. & Taylor, G. J. Graphite-Magnetite Aggregates in Ordinary Chondritic Meteorites. *Nature* 544–546 (1981).
38. Garvie, L. A. J. & Buseck, P. R. Nanosized carbon-rich grains in carbonaceous chondrite meteorites. *Earth Planet Sci Lett*. 431–439 (2004).
39. Young, A. J., Ross, R. R. & Fabian, A. C. Iron line profiles including emission from within the innermost stable orbit of a black hole accretion disc. *Monthly Not. R. Astronomical Soc.* **300**, L11–L15 (1998).
40. Mizuno, T., Ohmori, T. & Enyo, M. Isotopic changes of the reaction product induced by cathodic electrolysis in Pd. *J. N. Energy* **1**, 31 (1996).
41. Spurgeon, J. M. & Lewis, N. S. Proton exchange membrane electrolysis sustained by water vapor. *Energy Environ. Sci.* 2993–2998 (2011).

42. Bonitz, M. Quantum Kinetic Theory 249–250. (Springer, 2016).
43. Karabut, A. B. & Karabut, E. A. Experimental results on excess power, impurity nuclides, and X-ray production in experiments with a high-voltage electric discharge system. *Condens. Matter Nucl. Sci.* **8**, 41–47 (2012).
44. Pollack, G. H., Cameron, I. L. & Wheatley, D. N. Wheatley. Water and the Cell. SpringLink (2006).
45. Lbl, N., Puippe, J. C. & Angerer, H. Electrocrystallization in pulse electrolysis. *Surf. Technol.* **6**, 287–300 (1978).
46. Strachan, J. D. High-temperature plasma in a tokamak fusion test reactor. *Phys. Rev. Lett.* **58**, 1004 (1986).
47. Barut, A. O. & Bracken, A. J. Zitterbewegung and the internal geometry of the electron. *Phys. Rev. D.* **23**, 2454 (1981).
48. John, W. & Peters, A. New era for electron bifurcation. *Curr. Opin. Chem. Biol.* **47**, 32–38 (2018).
49. Lee, M. B. *Quantum Kinet. Well* **11/233**, 421 (2022).
50. Masha, R. T., Houreld, N. N. & Abrahamse, H. Low-intensity laser irradiation at 660 nm stimulates transcription of genes involved in the electron transport chain. *Photomed. Laser Surg.* **31**, 47–53 (2013).
51. Bonitz, M. Quantum Kinetic Theory. 14–19. (Springer, 2016).
52. Lee, M. B. *Quantum Kinet. Fusor* **17/005**, 663 (2021).
53. Pelletier, G. J., Lewis, E. & Wallace, D. W. R. CO2SYS. XLS: a calculator for the CO_2 system in seawater for Microsoft Excel/VBA. Version 24.
54. Li, X. Z., Tian, J., Mei, M. Y. & Li, C. X. Sub-barrier fusion and selective resonant tunneling. *Phys. Rev. C* **61**, 61 (2000).

ACKNOWLEDGEMENTS

This research was funded by QUANTUM KINETICS CORP. We thank Kathleen Munson, Chinmayee Subban, Regan Farrell, Ryan Sumner, and Peter Regier from the Pacific Northwest National Laboratory (PNNL) for contributing to sample analysis and consultation. PNNL is operated by Battelle for the U.S. Department of Energy under Contract DE-AC05–76RL01830. Part of this research was performed at the University of Washington, Molecular Analysis Facility (MAF). The MAF is part of the National Nanotechnology Coordinated Infrastructure (NNCI), a National Science Foundation-funded effort to coordinate nanoscale research and development activities across the United States and is supported by NNCI-2025489 and NNCI-1542101. The devices tested in this study are described in the following patents: Quantum Kinetic Oscillator (Heater): 20210095846 (Publication Date: 4/1/2021), Quantum Kinetic Fusor (Fusion): 20210156037 (Publication Date: 5/27/2021), Quantum Kinetic Well™ (Electronics): 17,228,925 (Issued: 1/25/2022 - Track-One), Quantum Kinetic Injector (Water Powered Cars): 2/20/2022 (Patent Pending).

AUTHOR CONTRIBUTIONS

Conceptualization, M.L., N.W., and R.K.; methodology, M.L., N.W., and R.K.; formal analysis, M.L.; investigation, M.L., N.W., and R.K.; resources, M.L.; data curation, M.L. and N.W.; writing—original draft preparation, M.L.; writing—review and editing, M.L., N.W., and R.K.; visualization, M.L., and N.W.; funding acquisition, M.L. All authors have read and agreed to the published version of the manuscript.

COMPETING INTERESTS

The authors declare no competing interests.

ADDITIONAL INFORMATION

Supplementary information The online version contains supplementary material available at https://doi.org/10.1038/s41545-022-00179-w.

Correspondence and requests for materials should be addressed to McKane B. Lee.

Reprints and permission information is available at http://www.nature.com/reprints

Publisher's note Springer Nature remains neutral with regard to jurisdictional claims in published maps and institutional affiliations.